Scintillating Zinc Oxide Ensconced in a Carbon Nanotube Forest Engineered by Laser Micro-Welding

Zhong Wei Isaac Kwek[a,+], *Yi Jie Valerie Tan*[a,+], *Zheng Zhang*[c], *Chorng-Haur Sow*[b,*], *Sharon Xiaodai Lim*[b,*]

[a] Dunman High School, 10 Tanjong Rhu Road, Singapore 436895

[b]Department of Physics, National University of Singapore, 2 Science Drive 3, Singapore 117542

[c]Institute of Materials Research and Engineering, A*STAR (Agency for Science, Technology and Research), 2 Fusionopolis Way, Innovis, Singapore 138634

*Address correspondence to Dr. Sharon Lim Xiaodai. Phone: (+65) 6516 1161. E-mail: phylimx@nus.edu.sg and Prof. Chorng Haur Sow. Phone: (+65) 65162957. Fax: (+65) 67776126. E-mail: physowch@nus.edu.sg

[+] The authors contributed equally to this work.

Abstract

Herein, we report defect-introduction *via* focused-laser-beam (FLB) modification to introduce carbon defects into zinc oxide (ZnO) thin film. The approach begins with a carbon nanotube (CNT) array covered by a thin layer of sputtered Zn on top of the array. When FLB irradiates the covered CNT array under ambient conditions, effective laser energy absorption by CNT results in ZnOCNT nanohybrid formation, it also enables site-selective transformation to be achieved. By adjusting the laser power, the degree of carbon incorporation into the pristine Zn system can be tuned and this exerts some degree of control over the fluorescent properties of the nanohybrid. Generating a higher defect density increases the intensity and changes the wavelength of the fluorescence emitted by ZnO under ultraviolet (UV) excitation and enhances its field emission properties. In particular, the turn-on electric field (E_{TO}) of the nanohybrid decreases. A lower E_{TO} reduces the probability of arc formation, a significant problem currently undermining the industrial feasibility of field emission displays (FED). Electron emission from these samples can be enhanced by exciting the laser-treated sample with an external laser source. The normalised current produced increases by as much as 6μA/(mW/mm^2) when the sample is excited by a 405nm monochromatic laser.

Keywords: Zinc oxide, carbon nanotubes, nanohybrid, field emission, focused laser beam

1. Introduction

Zinc oxide (ZnO), a wide bandgap material[1] (3.4eV), has long been identified as one of the most promising candidates for the creation of ultra-violet (UV) light-emitting diodes and laser diodes[2]. As a wide-bandgap semiconductor, ZnO is prone to having multiple native defects introduced into its bandgap. This high defect density is oft-deemed undesirable as it hinders the synthesis of p-type ZnO, which has useful electronic applications. On the other hand, through intentional defect-engineering and hybrid formation with other materials such as carbon, this particular material has been engineered to produce a broad spectrum of fluorescence wavelengths ranging from 390nm to 1000nm[3], widening its applications as a light-emitting source.

In particular, nanohybrids formed between ZnO and carbon nanotubes (CNT) have been the focus of several reports by virtue of their exceptional electrical properties. These are typically fabricated using: (a) physical mixing of both species, (b) physical deposition of one species onto the other and (c) chemical deposition of one species onto the other. Before their potential applications can be explored, further development of reliable and facile techniques to fabricate such nanohybrids and engineer their properties properly is necessary.

This work presents a simple technique to fabricate a hybrid comprising ZnO and multiwalled CNT (MWCNT), which shall hereafter be referred to as ZnOCNT. A sample comprising Zn film sputtered on top of an aligned array of MWCNT is irradiated by scanning focused laser beam (FLB) in ambient conditions. The efficient absorption of the laser beam by the MWCNT gives rise to a rapid increase in local temperature, stimulating chemical reactions among the different elements in the sample and oxygen molecules in the atmosphere that result in the rapid formation of ZnO. However, before a stable equilibrium is attained, the scanning FLB moves

away. The local region cools down rapidly, leaving the ZnO formed trapped in a quenched state and introducing defects into the ZnOCNT hybrid. The abundance of defects creates numerous interesting mid-bandgap energy levels, rendering the nanohybrid well-suited for band structure engineering. MWCNT play multiple indispensable roles in this dynamic process: (1) they rapidly absorb and convert the laser energy into the heat required for the chemical reactions to take place, (2) they serve as anchoring/housing matrices for the components of this quenched and disorderly system of materials and (3) in their competition with Zn for oxygen, they contribute to the formation of various defects in the system that contribute significant mid-bandgap energy states for active fluorescence emission.

Notwithstanding its disconformity with typical synthesis methods, this approach that relies on using a scanning FLB opens a wealth of possibilities for material engineering, including the creation of a wide variety of aesthetically pleasing micropatterns to accompany the functional applications of the nanohybrid.

The electrical properties of a nanohybrid formed *via* such combination as that of ZnO and CNT, both of which are favoured field emitters, was also a prime subject of our investigation. Detailed studies have already been reported on these nanostructured materials, independently[4-15] and in a hybrid formation[16-22]. However, except for one study that shed light on the ultrafast non-linear optical switching capabilities of CNTs beaded with ZnO nanoparticles[23], none have reported the photo-enhanced field emission effects exhibited by this unique hybrid.

As a possible application, the photo-enhanced field emission behaviour of the FLB-treated ZnOCNT nanohybrid is investigates by illuminating it with an external excitation source during the field emission process. The energy imparted to the sample triggers photo-enhanced field emission, allowing more electrons to be emitted under the same applied electric field. The

occurrence of this phenomenon is attributed to multiple effects of FLB modification, namely (1) the creation of ZnO nanoparticles with better crystallinity and more clearly defined edges, (2) the improvement in the aspect ratio of our nanohybrid, and (3) the introduction of sporadic defects which introduced mid-bandgap energy levels, allowing the nanocomposite to be responsive to external excitation.

2. Material and Methods

2.1 Growth of Multiwalled Carbon Nanotubes (CNTs)

CNTs with a typical length of 80μm, are grown on n-type silicon (Si) (~5mm x 5mm) substrates. Before growth, a layer of iron film is coated onto the substrates as a catalyst using a magnetron sputtering system (model: RF Magnetron Denton Discovery 18). The coating rate is 4nm $min^{-1,}$ and the coating duration is 3 mins. The CNTs array is synthesized using a plasma-enhanced chemical vapour deposition (PECVD) system. Details of the growth process are reported elsewhere.[24]

2.2 Formation of ZnCNT Hybrid

Zinc (Zn, 99% purity) is deposited onto the CNT array through direct current (DC) magnetron sputtering in an Argon (Ar) environment for 9 mins (model: RF Magnetron Denton Discovery 18). Details of the sputtering process is presented in the supporting information.

2.3 Further Characterizations

Further characterizations are carried out using a fluorescence microscope (FM) (model: Olympus BX51) under ultra-violet (UV, 300-390 nm), blue (B, 450-500 nm), green (G, 500-560 nm) and yellow (Y, 530-580 nm) excitation. Surface morphology, crystallinity, and chemical composition are characterised using SEM-EDX (JEOL JSM6700-F with Oxford Instruments X-Max^{N} 150 EDX detector); AFM (SPM-Bruker Dimension® ICON^{TM}); TEM

(JEOL JEM-2010F) and Thermo Fisher Scientific Theta Probe XPS system. Raman and photoluminescence (PL) are carried out using a Renishaw System coupled with a 532nm and 325nm laser, respectively. Field emission measurements (FE) are conducted using a homemade chamber connected to a Keithley 237 High Voltage Source-Measure Unit.

3. RESULTS AND DISCUSSION

3.1 Laser-initiated Selective Transformation from Zinc to Zinc oxide-CNT Hybrid

A thick Zinc (Zn) layer is deposited onto the carbon nanotubes (CNTs) array through a simple sputtering process. The process results in the formation of large clusters of Zn connecting individual strands of CNTs on the surface of the array (**Figure 1**(a-b)). The presence of Zn on the CNT array is further verified with the EDX elemental map of the Zn element (Figure 1(c)). Detailed characterisation of the Zn sputtered CNTs sample can be obtained from the supporting information, **Figure S1**. At this stage, interactions between these two materials mostly arise from Van der Waals forces. As illustrated in the schematic in Figure 1(d), a focused 532 nm continuous laser beam is employed to initiate localised integration of the two elements under ambient condition. The broad beam laser is reflected off two mirrors into a customised microscope.

The laser beam then passed through a beam splitter within the microscope and focused through a 100x lens onto the sample. The spot size of the focused laser beam has a diameter of 1μm. With the hybrid sample strategically positioned on a computerised stage, laser beam induced localised heating of the sample is tuned by varying both the power of the laser and the duration of the exposure (Figure 1(e)). The outcome of such a controlled but rapid thermal heating process leads to site-specific alterations of the optical properties of the hybrid material. The most notable alteration of the optical properties is the bright fluorescence. Alternatively, the sample can also be enclosed in a small gas chamber, thereby allowing the laser treatment

process to occur in a controlled environment (Figure 1(f)). The versatility of the patterning process, in which both laser power and patterning speed can readily be adjusted, enables a well-controlled multi-coloured fluorescence "Merlion" display to be achieved (Figure 1(g)). The "Merlion" is a mythical creature comprising a lion head with the body of a fish.

While randomly distributed regions of weak fluorescence along a single strand of ZnO nanowire have been previously reported[25], to the best of our knowledge, such site-specific, single-coloured, uniform and high-intensity fluorescence from ZnOCNT has not been reported before. The uniqueness of this hybrid material lies in the fact that when the same "Merlion" pattern is observed under bright field (BF) illumination (inset of Figure 1(g)), the region emitting violet fluorescence is not visible, leaving only the region emitting green fluorescence to be seen.

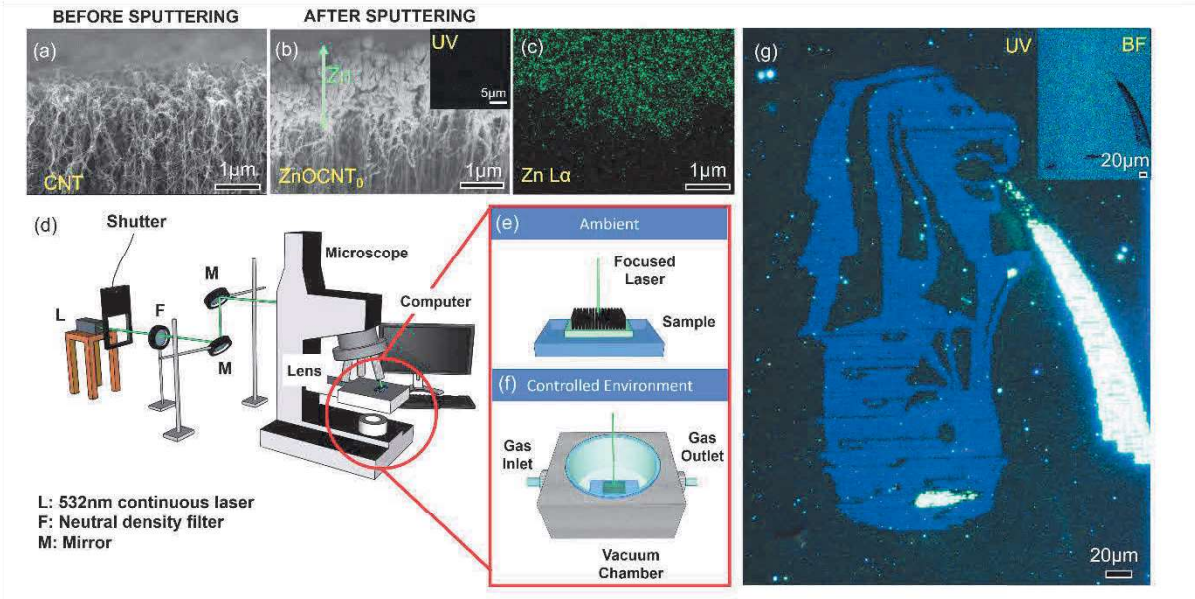

Figure 1. (a-b) Side view SEM image of the CNTs array before and after sputtering a layer of Zn on the surface of the array. (c) EDX elemental map of the Zn element from (b). (d) Schematic of focused laser beam system. (e-f) Laser patterning in (e) ambient and (f) gas chamber with attached gas inlets. (g) "Merlion" patterned structure highlighting the steganography capability of this process. Inset is the BF optical image from the same region.

Systematic studies were carried out to gain better insights into the bright fluorescence emitted by these hybrids. 30µm x 30µm square regions on the sample are modified using the following FLB powers: 7mW (8.9MW mm^{-2}), 9mW (11.5MW mm^{-2}) and 11mW (14.0MW mm^{-2}) with a patterning speed of 50 µm s^{-1}, and characterised using fluorescence microscopy (FM). The remarkable onset of intense fluorescence emission is evident in **Figure 2**(a-c). Under ultra-violet (UV, 300-390 nm) excitation, the pristine Zn coated CNT (ZnCNT) sample does not exhibit any distinct fluorescence (inset of Figure 1(b)). The sparse specks of fluorescence seen are drastically different from the concentrated and uniform fluorescence localised precisely within the modified square regions as depicted in Figure 2(a-c). The particular portions of the ZnOCNT nanohybrid emitting violet fluorescence, a mix of violet and green fluorescence, and green fluorescence will hereafter be referred to $ZnOCNT_V$ (Figure 2(a)), $ZnOCNT_{VG,}$ (Figure 2(b)) and $ZnOCNT_{G,}$ (Figure 2(c)) respectively. The laser powers 7mW, 9mW and 11mW were chosen because there was a change in the fluorescence colour from blue to green at 9mW. A systematic study on the impact of laser power and patterning speed on the fluorescing properties, together with the rationale for choosing 50 µm s^{-1} as the patterning speed can be obtained from supporting information (**Figure S2**).

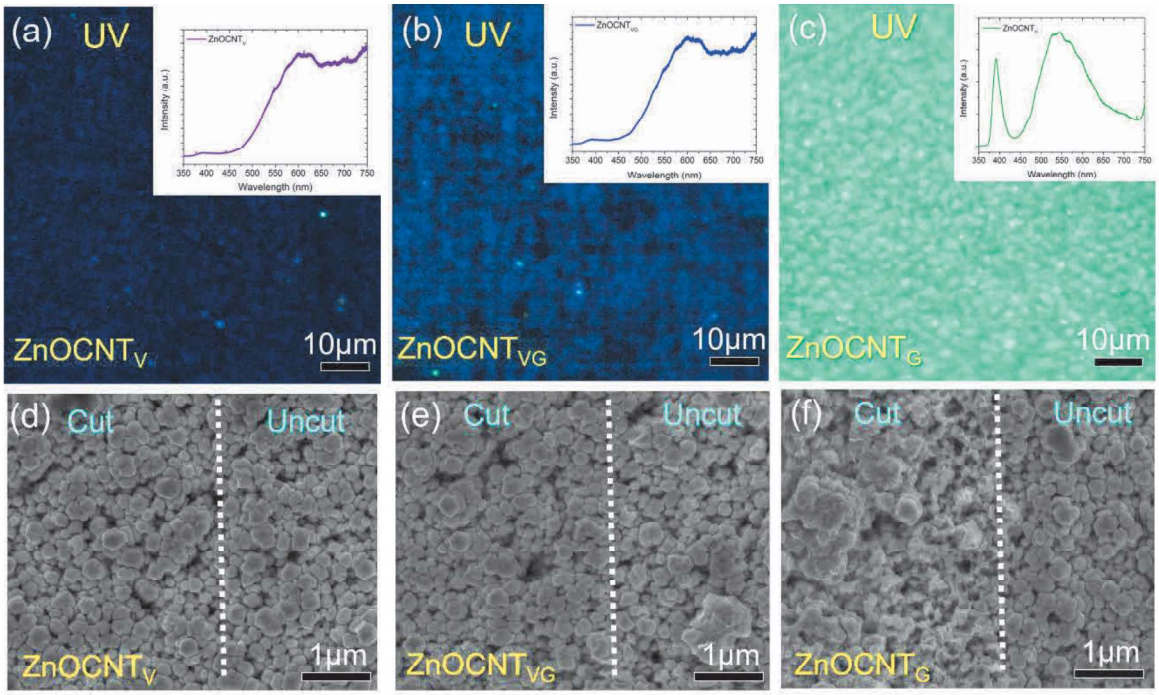

Figure 2. FM and SEM images of squares cut using laser powers of (a, d) 7mW, (b, e) 9mW, and (c, f) 11mW under ultraviolet (UV) excitation. Insets of (a-c) depict the respective PL spectrum of the individual samples.

The observed colour variations are also supported by spectra obtained from photoluminescence spectroscopy (PL, inset of Figure 2(a-c)). It is important to note that even at the submicron-scale level, the SEM image of the violet fluorescing region (Figure 2(d)) shows no significant differences between the physical morphologies of the laser-treated and pristine regions. The invisibility of the pattern strongly suggests the viability of using this hybrid system as a cost-efficient and hassle-free steganography material, as illustrated in the "Merlion" image of Figure 1(g).

3.2 TEM Analysis

TEM analysis of pristine Zn coated CNTs samples reveals large aggregation of Zn nanoparticles along different strands of CNTs (inset of **Figure 3**(a)). In the absence of visible lattice structures, the HRTEM of one such nanoparticle attached along a CNT strand (Figure 3(a)) suggests that the pristine hybrid material takes on an amorphous state. As the laser power increases from

7mW to 11mW, the transformation of the Zn layer sitting atop the CNT array to ZnO takes place. The crystallinity of the ZnO changes from amorphous in $ZnOCNT_V$ (Figure 3(b)) to clearly defined crystallinity in $ZnOCNT_G$ (Figure 3(d)). No lattice is observable from $ZnOCNT_V$ in the TEM images, while lattice spacing from $ZnOCNT_{VG}$ (Figure 3(c)) and $ZnOCNT_G$ (Figure 3(d)) correspond to the (100) plane (d = 2.84Å) (JCPDS 79-0208) and the (002) plane of wurtzite structure ZnO (d = 2.63Å) (JCPDS 79-0208). As the ionic radius of O^{2-} is smaller than that of Zn^{2+}, incorporating more O into the lattice structure will reduce the average interionic distance in the lattice. Thus, the decrease in the d-spacing indicates an increase in the O: Zn ratio in the hybrid as the laser power increases. The change in d-spacing suggests that the observed green fluorescence arises from the formation of a higher concentration of ZnO on top of the CNT array as the laser power increases.

3.3 Photoluminescence Spectroscopy

Respective PL spectra displayed as insets of Figure 2(a-c) are deconvoluted over the range from 350 nm to 440 nm (Figure 3(f-h)). The deconvoluted spectra show the presence of four peaks obtained from $ZnOCNT_V$ (Figure 3(f)) and $ZnOCNT_{VG}$ (Figure 3(g)) samples, while only three deconvoluted peaks are derived from the $ZnOCNT_G$ (Figure 3(h)) sample. Deconvoluted PL spectrum of pre-laser cut ZnCNT sample (plotted range, 350nm to 440nm) is also included in Figure 3(e), and the peak centres are determined to be located at 389nm and 405nm. Insets show the corresponding UV excited fluorescence images. The relative intensity of the highest peak from $ZnOCNT_{VG}$ and $ZnOCNT_G$ to $ZnOCNT_V$ is $I_{VG}/I_V = 1.39$ and $I_G/I_V = 591.38$. A possible contribution to the huge increase in relative emission intensity is highlighted in the following discussion. From the above observation, although there appears to be a transition of fluorescence from violet ($ZnOCNT_V$) to a random mix of violet and green ($ZnOCNT_{VG}$), incomplete transformation coupled with the use of a small laser spot during PL measurements result in similar PL spectra being detected from both samples. At room temperature, UV

emission from ZnO nanowires with PL peak centred between 367 nm -380 nm is often associated with the recombination of excitons.[1, 2, 25]

In our case, PL peak at 383 nm can also be attributed to such an effect. However, other peaks from 393 nm to 409 nm are likely due to other forms of transitions. As laser power increases, we observe recombination of the original 383 nm and 393 nm peaks, resulting in detecting a single peak at 390 nm. At the same time, peaks at 403 nm remain unchanged while the peak at 409 nm experiences a blue shift towards 404 nm. The presence of PL peaks associated with violet emission from ZnO has been attributed to two transitions of electrons, which take place between (1) the acceptor of Zn vacancy and the conduction band and (2) the donor of oxygen vacancy to the valence band.[1, 26] Both account for a redshift of 35 nm – 45 nm of the PL peak produced *via* exciton recombination. In our case, the shift experienced is too small to be attributed to such transitions between donor, acceptor, and the respective conduction, valence bands, and likely stems from the presence of C from CNTs supporting the pristine Zn film or strained within the system contributed by sudden quenching of the disorder system upon removal of the laser source.

3.4 Raman Spectroscopy

Possible interactions between C and ZnO are captured and presented in Raman spectra of ZnCNT, $ZnOCNT_V$, $ZnOCNT_{vG}$, and $ZnOCNT_G$ (Figure 3(i-l)). In general, as laser power increases, noticeable dissociation of peaks between 400-570cm^{-1} takes place. The revelation of the peak at 563 cm^{-1}, a downward shift from the usual detection range of 574-579 cm^{-1},[27-30] provides concrete evidence of strong interactions between ZnO and C in the CNTs.[31] Detection (Figure 3(k)) and enhancement in intensities (Figure 3(l)) of carbon-related D (1356 cm^{-1}), G (1580 cm^{-1}), 2D (2693 cm^{-1}) and D' (2919 cm^{-1}) peaks as laser power increases suggest possible ZnO to carbon interactions, in which ZnO likely serves as a surface-enhanced Raman

scattering (SERS) substrate.[31] It could also be attributed to the exposure of underlying CNTs with the removal of ZnO by the laser (Figure 2(f)).

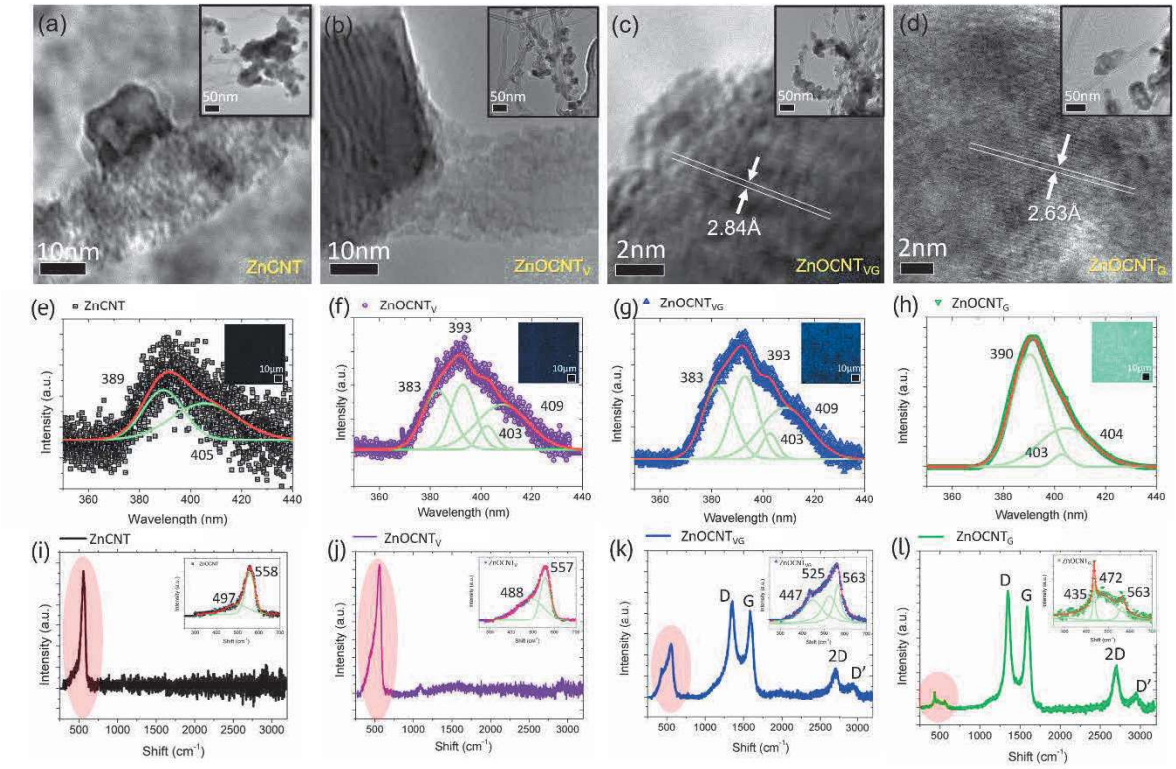

Figure 3. High resolution transmission electron microscopy (HRTEM) images of (a) ZnCNT, (b) ZnOCNTV, (c) ZnOCNTVG and (d) ZnOCNTG. Insets are TEM images of the respective samples. (e-h) Photoluminescence spectra and (i-l) Raman spectra of (e, i) ZnCNT, (f, j) ZnOCNTV, (g, k) ZnOCNTVG and (h, l) ZnOCNTG. Insets of (e-h) fluorescence images under UV excitation. Inset of (i-l) shows fitted data of the peak enclosed within the red ovals (i-l).

3.5 XPS Analysis

Chemical compositions of ZnCNT (Figure S3), ZnOCNTv (**Figure 4**(a-c)), ZnOCNTVG (Figure 4(d-f)) and ZnOCNTG (Figure 4(g-i)) are analysed *via* X-Ray photoelectron spectroscopy (XPS). C 1s measurements from these samples show the formation of more C=O and O-C-O bonds from ZnOCNTVG (Figure 4(d)), where the transition from violet to green fluorescence takes place. The formation of strong covalent single and double bonds between carbon and oxygen atoms is consistent with other metal oxides/C.N.T. composite materials.[32, 33] The results from the O 1s and Zn $2p_{3/2}$ spectra confirm the presence of higher O-Zn concentration in ZnOCNTG (Figure 4(h)) compared to ZnOCNTV (Figure 4(b)). The O 1s peak at 530.6 eV

is attributed to O_2^- in the ZnO crystal lattice, and the Zn $2p_{3/2}$ peak at 1022 eV is attributed to Zn^{2+} in the ZnO crystal lattice. By calculating the areas under these peaks across all the spectra, the quantity of the chemical bonds they represent can be determined. Base on the above calculation, the ratio of peak area of O-Zn peak of $ZnOCNT_G$ to ZnCNT is 32% higher than the ratio of O-Zn peak of $ZnOCNT_{VG}$ to ZnCNT. It is also 110% higher than the ratio of the O-Zn peak of $ZnOCNT_V$ to ZnCNT.

Similarly, the ratio of peak area of Zn $2p_{3/2}$ peak in $ZnOCNT_G$ to ZnCNT is 20% higher than the ratio of peak area of Zn $2p_{3/2}$ peak of $ZnOCNT_{VG}$ to ZnCNT. It is also 49% higher than the ratio of Zn $2p_{3/2}$ peak of $ZnOCNT_V$ to ZnCNT. As laser power increases, a shift towards lower binding energy by 0.3 eV of the Zn $2p_{3/2}$ peak is observed. No Zn-C bonding has been detected from the hybrid materials. Nevertheless, based on the XPS results, the presence of -Zn-O-C bonds in our hybrid material is expected. Bond formation of this form has been reported in other metal oxides/C.N.T. composite materials.[3, 34, 35] The confluence of XPS results, Raman spectroscopy measurements, and literature studies strongly support the claim that the higher intensity of the green fluorescence emitted by $ZnOCNT_G$ vis-à-vis that of $ZnOCNT_{VG}$ arises from an increase in the ZnO concentration. In other words, one can consider the state of $ZnOCNT_V$ to be the tipping point at which the transformation is about to take place. At $ZnOCNT_{VG}$, the transformation is in the process of taking place, and at the state of $ZnOCNT_G$, an effective transformation from Zn to ZnO and increased formations of -Zn-O-C bonds has taken place. The final transformation results in a tremendous increase in fluorescence intensity of about 600 times from the hybrid material.

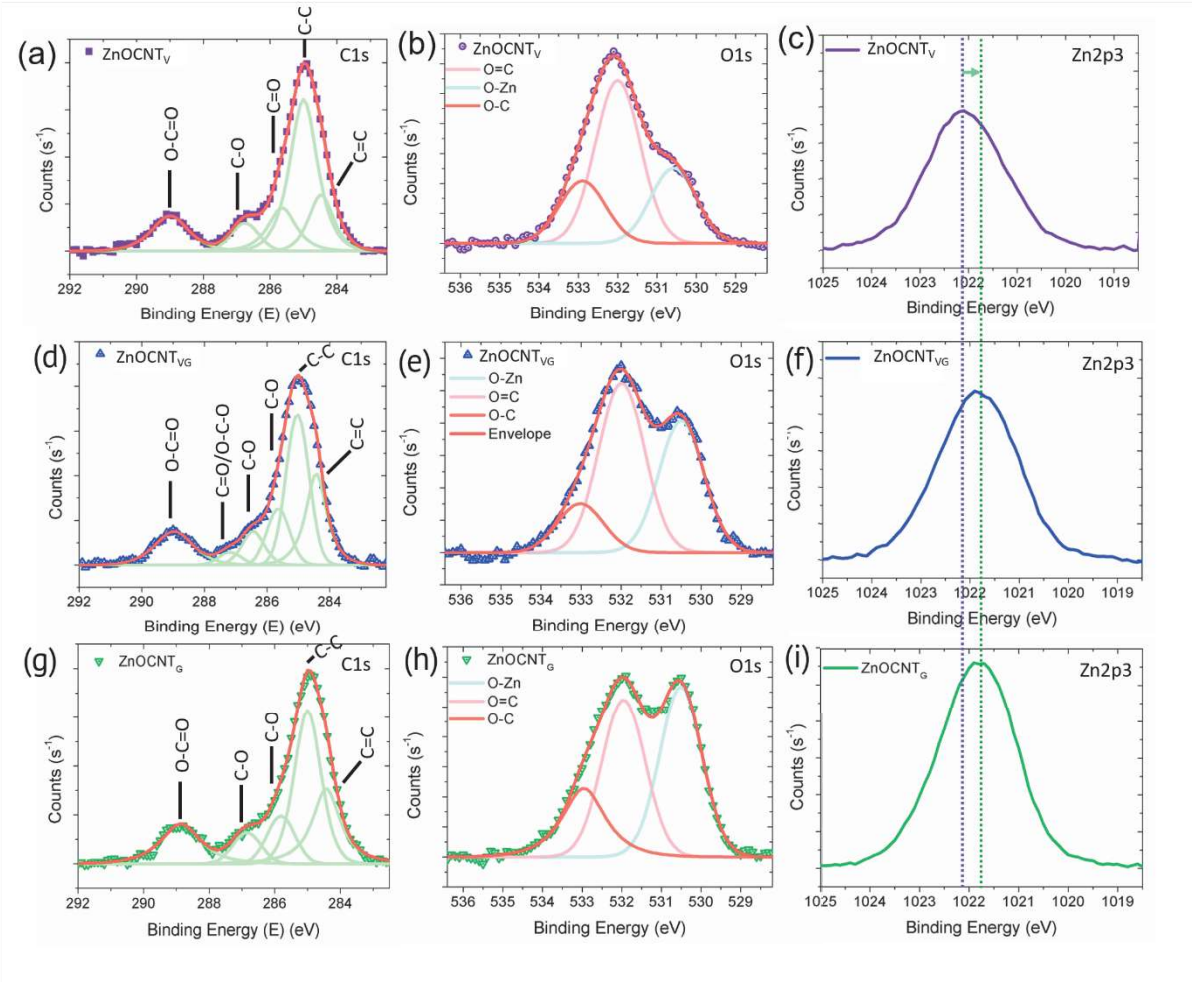

Figure 4. X-ray photoelectron spectroscopy (XPS) spectra from (a-c) $ZnOCNT_V$, (d-f) $ZnOCNT_{VG}$, and (g-i) $ZnOCNT_G$.

3.6 Proposed Mechanism for Laser Initiated Fluorescence in the Hybrid Structure

Factors contributing to the changes in the observed fluorescence are determined through a series of low-temperature studies. The temperature of the laser-treated sample is lowered, while fluorescence images and emission spectra are collected using an FM The suppression of non-radiative electron-hole recombination processes enables radiative electron-hole recombination processes to occur more readily. By resolving the corresponding fluorescence emitted, specific defect states can be identified.

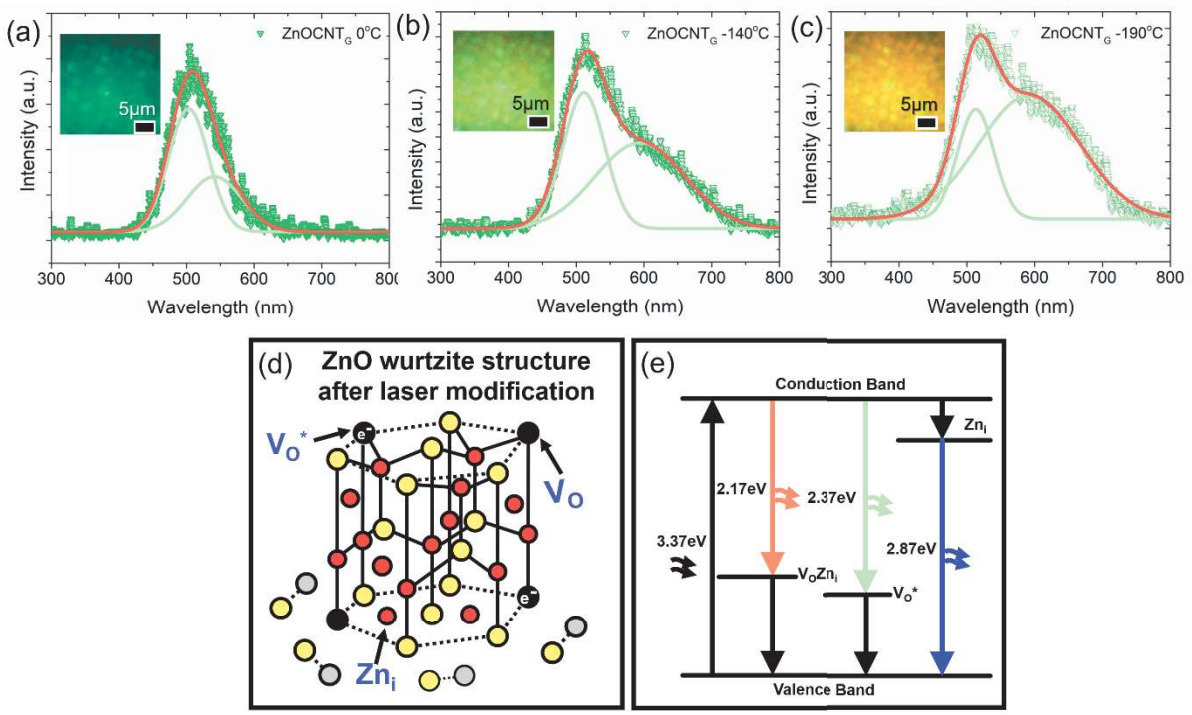

Figure 5. (a)-(c) Fluorescence spectra ZnOCNT$_G$ at (a) 0°C, (b) -140°C, (c) -190°C. The insets of (a)-(c) are the corresponding FM images of the nanohybrids under UV excitation. (d) Schematic of the ZnO wurtzite after laser treatment. (e) Possible de-excitation paths of excited electrons, which results in the range of fluorescence observed.

At 0°C, the spectrum can be deconvoluted into two gaussian graphs with a peak position at ~503nm and ~541nm, respectively (**Figure 5**(a)). The ratio of the area under these two peaks is 1.62. As the temperature decreases from 0°C to -140°C, both peaks exhibit redshift from ~503nm to ~511nm and ~541nm to ~594nm. The above results agree with the corresponding FM image (inset of Figure 5(b)) given the presence of bright green speckles and a touch of yellow fluorescence. The ratio of the areas under these two peaks now has a value of 0.73. Lowering the temperature from -140˚C to -190˚C (Figure 5(b,c)) results in a significant reduction of the peak area ratio to 0.32, while the peak positions remain at ~513nm (~2.42eV) and ~592nm (2.09eV) respectively. These peaks correspond to the energy levels of O vacancy-Zn interstitial (V_o-Zn_i) clusters[36] and interstitial O vacancies (O_i)[37], respectively. The reduction of peak areas ratio agrees with the redshift in the fluorescence emitted as temperature reduces. These trends are attributed to the fact that lowering the temperature leads to

suppressing non-radiative electron-hole recombination processes. Such suppression enables radiative electron-hole recombination processes to occur more frequently, and the intensity of the corresponding fluorescence emitted to increase and be detected more easily. This emphasises the important role that defects play in contributing to the observed green fluorescence.

3.6.1 Yellow fluorescence (~592nm)

Conventional methods of incorporating Zn_i into ZnO single crystals involve heating them in Zn vapour, followed by rapid quenching. This process bears a striking resemblance to laser-pruning, which dissociates a portion of the Zn thin film by channelling a substantial amount of energy to it. As the laser beam only encounters the Zn thin-film momentarily, this energy transfer is transient. It is followed by the rapid cooling of the material, causing the newly introduced Zn to be trapped within the ZnO wurtzite lattice, thereby resulting in the formation of Zn_i. Figure 5(d) depicts such a scenario. Apart from the possible bond formation of -Zn-O with C, we believe that C serves multiple crucial purposes in the observed phenomenon. These roles are determined through a series of experiments.

Firstly, FLB patterning is carried out on sputtered Zn film without (Figure S4(a)) and with (Figure S4(b)) CNTs. FM and SEM images of the squares presented in Figure S4 show that in the absence of CNTs, green fluorescence is not observed from the ZnSi sample – highlighting the vital contribution that C has in creating the observed green fluorescence from the ZnOCNT samples. Secondly, FLB with the same laser power is used to modify a similar CNT array coated with a thinner Zn layer (Figure S4(c-d)). When the thickness of the Zn layer is reduced, heat from the laser is more readily absorbed by the underlying CNTs, resulting in the observation of green fluorescence from the patterned region. The above results suggest that the CNTs array could also be playing the role of a heat source. It readily absorbs energy from the laser beam,

raising the localised temperature of the Zn film and initiating a chain of chemical reactions. In CNT in vacuum, FLB heating can increase the localised temperature up to ~2500k.[38]

The Raman spectra substantiate the critical role of C in Figure 3(i-l). The disordered (D) carbon peak at ~1350 cm^{-1} and the graphite (G) peak at ~1578 cm^{-1} are absent from the Raman spectrum of $ZnOCNT_V$ but present in that of $ZnOCNT_{VG}$. The intensities of these peaks increase from $ZnOCNT_{VG}$ to $ZnOCNT_G$. Moreover, the higher intensity of the D peak vis-à-vis the G peak (I_D/I_G ratio ($ZnOCNT_{VG}$): 1.0447; I_D/I_G ratio ($ZnOCNT_G$): 1.0117) in the Raman spectra of $ZnOCNT_{VG}$ and $ZnOCNT_G$ indicates the presence of more disordered carbon than graphitic carbon in both hybrids. The above result is likely due to the formation of bonds between C and O. When ablated at low laser powers, the ZnO thin film prevents CNTs from being exposed. The ZnO thin film thus hinders the detection of the C signal by the machine. As the laser power increases, the ablation of ZnO increases, exposing more CNTs and increasing their surface area in contact with atmospheric O. The presence of C from CNT allows Zn-Zn bonds to be more readily broken,[39] thereby facilitating the formation of C=O bonds under intense heating by the FLB.

The formation of C=O bonds, in turn, causes some of the spaces intended for occupation by O within the ZnO wurtzite structure to be vacant, giving rise to V_o. Lending credence to this theory is the fact that the C=O peak area in the O1s XPS spectra of $ZnOCNT_G$ is more significant than that of $ZnOCNT_V$, attesting to the fact that C reacts with atmospheric O during laser-pruning to form C=O bonds. C contributes significantly, albeit indirectly, to the generation of the green luminescence by removing O from the ZnO structure. As deep level defects, V_o and Zn_i form a defect cluster. The recombination of an electron at the V_o-Zn_i cluster energy level and a hole at the valence band maximum (VBM) give rise to the emission of yellow fluorescence.

Furthermore, the presence of C within the hybrid system allows it to be readily incorporated into the ZnO matrix, which can also contribute to the observed yellow fluorescence.[25]

3.6.2 Green fluorescence (513nm)

On the other hand, the formation of Vo is caused by the oxidation of Zn during laser-pruning, which results in electrons occupying the vacant O spaces in the lattice structure. The recombination of a hole at VBM with V_o leads to the emission of green fluorescence at 513nm. This proposal is verified by conducting FLB patterning in an inert (helium, He) environment with a pressure of $7x10^{-3}$ Torr. The process is carried out by placing the sample in a vacuum chamber and filling it with He gas. It is observed from the FM images in Figure S5(a-c) that the various luminescence previously observed under ambient condition (Figure S5(g-i)) is no longer visible. SEM images of the laser-treated region using 7mW and 9mW shows negligible differences between the two samples treated in He (Figure S5(d-f)) and ambient (Figure S5(j-l)) condition. However, it is noticeable that using 11mW; almost all the Zn layers are removed from the patterned region in He (Figure S5(f)).

In contrast, on the sample treated in ambient conditions, ZnO structures are visible (Figure S5(l)). The above observation seems to run counter to the previous conclusion that V_o is responsible for the green luminescence because while carrying out laser-pruning in an O-deficient environment would seem to increase the formation of V_o and thus increase the intensity of the green fluorescence produced, this phenomenon does not occur. It is postulated that this could be due to the lack of formation of ZnO in the O-depleted environment.

3.6.3 Violet fluorescence (393-390nm) and blue (403-409nm)

Observation of violet and blue fluorescence from the laser-treated sample could be due to the following. The violet fluorescence likely originates from band edge emission, which

corresponds to the bandgap energy of 3.2eV of ZnO. Band edge emission is often associated with the high crystallinity of ZnO. However, TEM images of our samples with green emission show that they have higher crystallinity than the violet fluorescing ones that were treated with lower laser powers. A closer look at the PL spectra reveals that violet and blue fluorescence are detected in all three types of samples. For samples treated with higher laser power, these violet and blue emissions are likely overshadowed by defects that initiated strong green emission. After considering the scenarios mentioned above, we propose the presence of multiple de-excitation paths for the excited electrons, which results in the observed fluorescence. These paths are depicted in Figure 5(e).

3.7 Application: Photo-enhanced Field Emission

In light of the strong field-emitting properties of ZnO and CNTs individually and the strong response of the ZnOCNT nanohybrid to photo-excitation, it is postulated that the nanohybrid is an ideal candidate for use in photo-enhanced field emission (FE). Variation in the field emission current density (J) produced by the four nanohybrids, namely $ZnOCNT_V$, $ZnOCNT_{VG}$, $ZnOCNT_G$, and ZnCNT, with an electric field (E) was studied. Schematic of the photo-enhanced FE setup is shown in **Figure S6**(a-b).

Under an applied electric field of 1.05V μm^{-1} (**Figure 6**(a)), $ZnOCNT_G$ produces the highest maximum current density (3.62mA cm^{-2}), followed by $ZnOCNT_{VG}$ (1.83mA cm^{-2}), ZnCNT (0.31mA cm^{-2}) and $ZnOCNT_V$ (0.01mA cm^{-2}). A similar trend is observed across the turn-on electric fields (which correspond to a current density of 0.1mA cm^{-2}) of the nanohybrids, with $ZnOCNT_G$ requiring the lowest turn-on field (0.85 V μm^{-1}), followed by $ZnOCNT_{VG}$ (0.86 V μm^{-1}), ZnCNT (0.97 V μm^{-1}) and $ZnOCNT_V$ (1.16 V μm^{-1}). A detailed discussion of the mechanism behind the observed field emission effect and the field emission current *vs* voltage plots of the respective samples are presented in **Section S7** in supporting information.

Plotting $\ln(J/E^2)$ to 1/E (termed as an Fowler-Nordheim (FN) plot, inset of Figure 6(a)), the enhancement factor or work function of the material can be determined from the gradient of the graph. Details of the calculation process can be obtained from **Section S8** of the supporting information. UPS analysis (**Figure S9**) of the samples allow individual work function the samples to be determined. The value of the respective work function is obtained through extrapolation at the cut-off point of the UPS spectra (inset in Figure S6). From this, the work function of ZnCNT, $ZnOCNT_V$, $ZnOCNT_{VG}$ and $ZnOCNT_G$ is determined to be 4.15 ± 0.002 eV, 4.17 ± 0.005 eV, 4.22 ± 0.006 eV and 4.20 ± 0.005 eV respectively. Combining the work function and the gradient of the respective graphs in the FN plot, enhancement factors of ZnCNT, $ZnOCNT_V$, $ZnOCNT_{VG,}$ and $ZnOCNT_{G,}$ are calculated to be $1.25x10^8$, $9.72x10^8$, $1.43x10^8$, and $2.88x10^{8,}$ respectively. Due to the superior field emitting properties of $ZnOCNT_{VG}$ and $ZnOCNT_G$, a further experiment is conducted to investigate their potential as photo-enhanced field emitters.

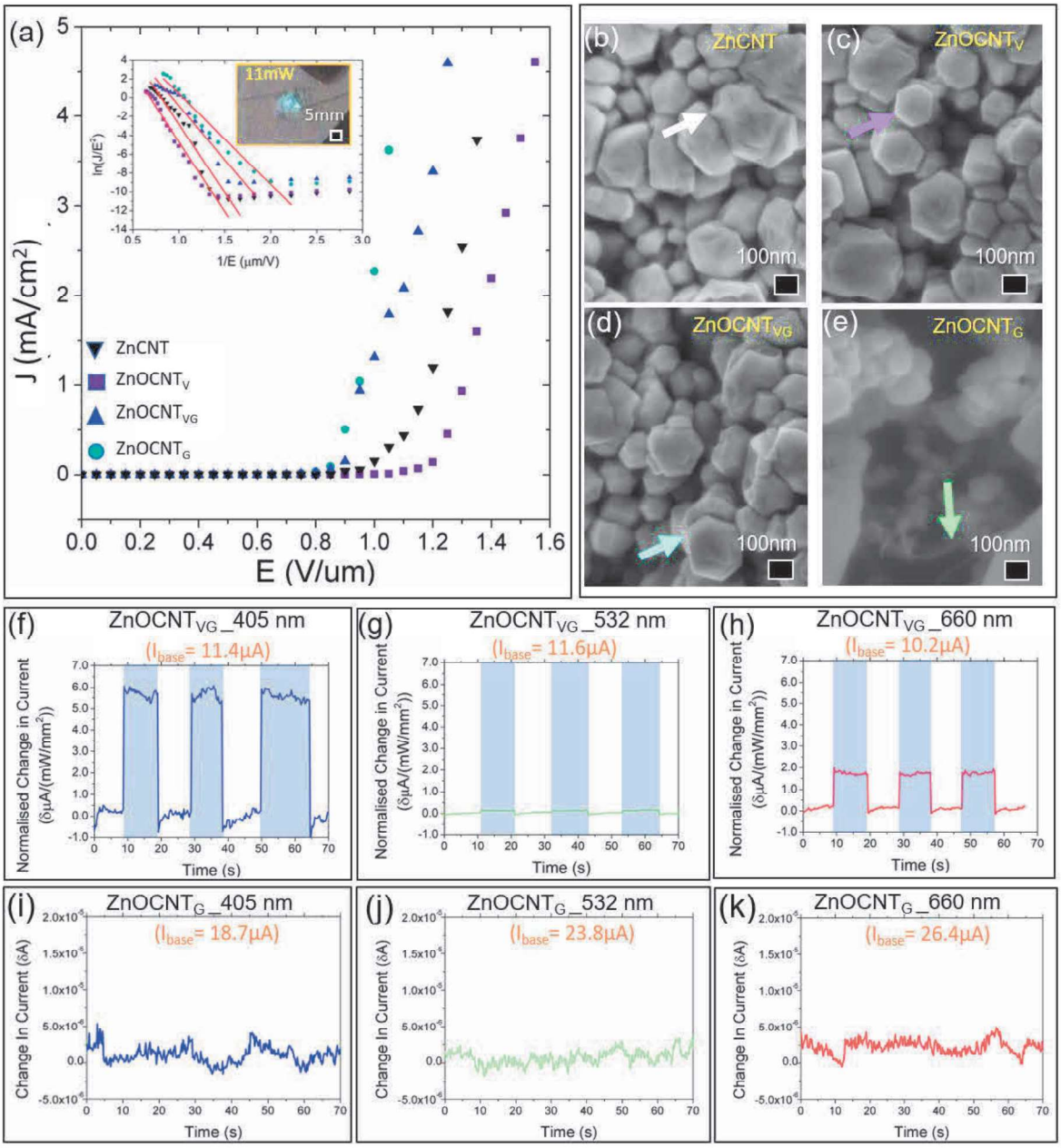

Figure 6. (a) Current density (J) against electric field (E) plot. Inset of (a) shows the FN plot for ZnCNT, $ZnOCNT_V$, $ZnOCNT_{VG}$, $ZnOCNT_G$ and an optical image showing fluorescing emission sites from the 11mW laser treated sample. (b)-(e) Top-view SEM images of (b) ZnCNT, (c) $ZnOCNT_V$, (d) $ZnOCNT_{VG}$ and (e) $ZnOCNT_G$. Current-time (I-t) plots of (f-h) $ZnOCNT_{VG}$ and (i-k) $ZnOCNT_G$ under photoexcitation of wavelength (f, i) 405nm, (g, j) 532nm and (h, k) 660nm.

While undergoing the field emission process, at a fixed applied voltage of 300V, the samples are excited by 405nm, 532nm, and 660nm laser with beam intensities of 2.3mW mm^{-2}, 30.9mW mm^{-2}, and 9.0mW mm^{-2}, respectively. Figure 6(f-k) show the photo-enhanced FE plots and base current when the external laser excites the samples at 10s intervals. It can be observed that

the field emission current (normalised to the excitation laser power density) emitted by $ZnOCNT_{VG}$ increases sharply under laser excitation (Figure 6(f-h)). In contrast, a similar normalised current from the $ZnOCNT_G$ sample does not exhibit any distinct increase when it is excited by the laser beam (Figure 6(i-k)). Detailed analysis of the results from $ZnOCNT_{VG}$ suggests that photo-enhanced field emission current is more readily generated by 405nm and 660nm laser.

A possible mechanism to the observed phenomenon could be the following: all three laser wavelengths can excite electrons in $ZnOCNT_{VG}$. However, the 405nm laser provides more energy for the electrons to be excited closer to the conduction band, thereby allowing these electrons to tunnel out of $ZnOCNT_{VG}$ more readily than 532nm and 660nm laser excitation. Although 660nm laser provided lesser energy for electron excitation, it is more easily absorbed by underlying carbon nanotubes[40], which could have enhanced current emission through an additional thermal process.

The inability of $ZnOCNT_G$ to produce photo-enhanced field emission can be attributed to the following: under the influence of an applied field, electrons readily tunnel out of the sparsely distributed ZnO nanoparticles. However, once emitted, electrons closer to the exposed CNTs (indicated by the green arrow in Figure 6(e)) could be trapped by the presence of more disordered defects within the CNTs. The more disordered defects are underscored by the high I_D/I_G ratio of 1.011 from the Raman spectra presented in Figure 3(l). As a result, the enhancement is no longer significant.

4. Conclusion

We have verified the viability of laser-pruning as a method of modifying the optical and field emission properties of ZnOCNT in an economical and resource-efficient manner. The

versatility of this technique renders it a significant edge over existing methods used to synthesise this particular nanohybrid. Further, our success in producing an "invisible" violet fluorescing pattern on our nanocomposite *via* FLB modification attests to the potential to leverage upon the combination of the intrinsic properties of the nanohybrid and the simplicity of FLB modification for cost-efficient steganography. The emission mechanism of the violet/blue, green, and yellow luminescence of ZnOCNT has been investigated. We propose that the observed fluorescence is due to the effects of incorporating oxygen vacancies, zinc interstitial, and carbon defects into the nanocomposite. Applications-wise, the ZnOCNT hybrid created has great potential to be used as a field emitter (with photo-enhanced capabilities initiated by exposure to 660nm and 405nm monochromatic light sources). By assessing the effect of changing the composition of Zn, O, and C in the ZnOCNT nanohybrid *via* laser-pruning on its field emitting properties as well as on its response to photo-excitation during field emission, our work has built on and enhanced existing research on the field emission properties of ZnOCNT hybrid as well.

Supporting Information

Supporting information is available online or from the author.

Acknowledgements

The authors acknowledge the generous support of the Singapore MOE-ARC grant (R-144-000-417-114). The authors thank Dr Kim Yong Lim for the insightful discussion about this work.

Notes

The authors declare no competing financial interest.

Reference

[1] M. Ramani, S. Ponnusamy, C. Muthamizhchelvan, Zinc oxide nanoparticles: A study of defect level blue-green emission, Optical Materials, 34 (2012) 817-820.
[2] P.A. Rodnyi, I.V. Khodyuk, Optical and luminescence properties of zinc oxide (Review), Optics and Spectroscopy, 111 (2011) 776-785.
[3] B. Aissa, C. Fauteux, M.A. El Khakani, D. Therriault, Structural and photoluminescence properties of laser processed ZnO/carbon nanotube nanohybrids, Journal of Materials Research, 24 (2009) 3313-3320.
[4] S. Fujii, S. Honda, H. Kawai, K. Ishida, K. Oura, M. Katayama, Effect of arrangement of pillar array of aligned carbon nanotube bundles on its field-emission characteristic, Diamond and Related Materials, 17 (2008) 556-558.
[5] S.K. Srivastava, V.D. Vankar, V. Kumar, V.N. Singh, Effect of substrate morphology on growth and field emission properties of carbon nanotube films, Nanoscale Research Letters, 3 (2008) 205-212.
[6] Y.W. Zhu, F.C. Cheong, T. Yu, X.J. Xu, C.T. Lim, J.T.L. Thong, Z.X. Shen, C.K. Ong, Y.J. Liu, A.T.S. Wee, C.H. Sow, Effects of CF4 plasma on the field emission properties of aligned multi-wall carbon nanotube films, Carbon, 43 (2005) 395-400.
[7] S. Fujii, S. Honda, H. Machida, H. Kawai, K. Ishida, M. Katayama, H. Furuta, T. Hirao, K. Oura, Efficient field emission from an individual aligned carbon nanotube bundle enhanced by edge effect, Applied Physics Letters, 90 (2007).
[8] J.H. Zhang, T. Feng, W.D. Yu, X.H. Liu, X. Wang, Q. Li, Enhancement of field emission from hydrogen plasma processed carbon nanotubes, Diamond and Related Materials, 13 (2004) 54-59.
[9] S.Y. Chen, H.Y. Miao, J.T. Lue, M.S. Ouyang, Fabrication and field emission property studies of multiwall carbon nanotubes, Journal of Physics D-Applied Physics, 37 (2004) 273-279.
[10] P.J. Cao, Y.S. Gu, F. Liu, H.W. Liu, H.R. Zhang, F. Shen, Q.F. Zhang, D.Y. Zhong, J.Q. Li, S. Liu, H.J. Gao, Fabrication of carbon nanotube bundles and measurement of field electron emission properties, Applied Physics a-Materials Science & Processing, 80 (2005) 195-199.
[11] C.C. Chiu, T.Y. Tsai, N.H. Tai, Field emission properties of carbon nanotube arrays through the pattern transfer process, Nanotechnology, 17 (2006) 2840-2844.
[12] Y.W. Zhu, X.D. Lim, M.C. Sim, C.T. Lim, C.H. Sow, Versatile transfer of aligned carbon nanotubes with polydimethylsiloxane as the intermediate, Nanotechnology, 19 (2008).
[13] J. Xiao, G.M. Zhang, X. Bai, L.G. Yu, X.Y. Zhao, D.Z. Guo, Field emission from zinc oxide nanostructures and its degradation, Vacuum, 83 (2008) 265-272.
[14] C.X. Xu, X.W. Sun, Field emission from zinc oxide nanopins, Applied Physics Letters, 83 (2003) 3806-3808.
[15] Z.L. Wang, Ten years' venturing in ZnO nanostructures: from discovery to scientific understanding and to technology applications, Chinese Science Bulletin, 54 (2009) 4021-4034.
[16] Y.S. Min, E.J. Bae, U.J. Kim, W. Park, C.S. Hwang, Direct growth of single-walled carbon nanotubes on conducting ZnO films and its field emission properties, Applied Physics Letters, 89 (2006).
[17] J.Y. Pan, C.C. Zhu, Y.L. Gao, Enhanced field emission characteristics of zinc oxide mixed carbon nano-tubes films, Applied Surface Science, 254 (2008) 3787-3792.
[18] X.B. Yan, B.K. Tay, Y. Yang, W.Y.K. Po, Fabrication of three-dimensional ZnO-Carbon nanotube (CNT) hybrids using self-assembled CNT micropatterns as framework, Journal of Physical Chemistry C, 111 (2007) 17254-17259.
[19] X.B. Yan, B.K. Tay, P. Miele, Field emission from ordered carbon nanotube-ZnO heterojunction arrays, Carbon, 46 (2008) 753-758.

[20] C.S. Huang, C.Y. Yeh, Y.H. Chang, Y.M. Hsieh, C.Y. Ku, Q.T. Lai, Field emission properties of CNT-ZnO composite materials, in: 2nd International Conference on New Diamond and Nano Carbons, Elsevier Science Sa, Taipei, TAIWAN, 2008, pp. 452-456.
[21] Y.M. Ho, W.T. Zheng, Y.A. Li, J.W. Liu, J.L. Qi, Field Emission Properties of Hybrid Carbon Nanotube-ZnO Nanoparticles, Journal of Physical Chemistry C, 112 (2008) 17702-17708.
[22] S. Zuo, X. Li, W.H. Liu, Y.N. He, Z.H. Xiao, C.C. Zhu, Field Emission Properties of the Dendritic Carbon Nanotubes Film Embedded with ZnO Quantum Dots, Journal of Nanomaterials, (2011).
[23] Y.W. Zhu, H.I. Elim, Y.L. Foo, T. Yu, Y.J. Liu, W. Ji, J.Y. Lee, Z.X. Shen, A.T.S. Wee, J.T.L. Thong, C.H. Sow, Multiwalled carbon nanotubes beaded with ZnO nanoparticles for ultrafast nonlinear optical switching, Advanced Materials, 18 (2006) 587-+.
[24] K.Y. Lim, C.H. Sow, J.Y. Lin, F.C. Cheong, Z.X. Shen, J.T.L. Thong, K.C. Chin, A.T.S. Wee, Laser pruning of carbon nanotubes as a route to static and movable structures, Advanced Materials, 15 (2003) 300-303.
[25] K.Y. Lim, J.J. Linghu, X. Chi, K.D. Yuan, K.M. Hew, M.R. Zheng, M. Yang, E.S. Tok, A. Rusydi, X.J. Yu, W. Chen, Y.P. Feng, C.H. Sow, Tunable Fluorescence Properties Due to Carbon Incorporation in Zinc Oxide Nanowires, Advanced Optical Materials, 5 (2017).
[26] Z.X. Fu, C.X. Guo, B.X. Lin, G.H. Liao, Cathodoluminescence of ZnO films, Chinese Physics Letters, 15 (1998) 457-459.
[27] B.H. Bairamov, A. Heinrich, G. Irmer, V.V. Toporov, E. Ziegler, RAMAN-STUDY OF THE PHONON HALFWIDTHS AND THE PHONON PLASMON COUPLING IN ZNO, Physica Status Solidi B-Basic Research, 119 (1983) 227-234.
[28] T.C. Damen, S.P.S. Porto, B. Tell, RAMAN EFFECT IN ZINC OXIDE, Physical Review, 142 (1966) 570-&.
[29] C.A. Arguello, D.L. Rousseau, S.P.S. Porto, FIRST-ORDER RAMAN EFFECT IN WURTZITE-TYPE CRYSTALS, Physical Review, 181 (1969) 1351-&.
[30] M. Koyano, P. QuocBao, L.T. ThanhBinh, L. HongHa, N. NgocLong, S. Katayama, Photoluminescence and Raman spectra of ZnO thin films by charged liquid cluster beam technique, Physica Status Solidi a-Applications and Materials Science, 193 (2002) 125-131.
[31] M.M. Hossain, H. Shima, M.A. Islam, M. Hasan, M. Lee, Synergetic Effect in Raman Scattering of ZnO Nanoparticles in ZnO-CNT Fibers: A Way To Enhance the G and 2D Band, Journal of Physical Chemistry C, 120 (2016) 17670-17682.
[32] Y. Shan, L. Gao, Synthesis and characterization of phase controllable ZrO2-carbon nanotube nanocomposites, Nanotechnology, 16 (2005) 625-630.
[33] L. Chen, B.L. Zhang, M.Z. Qu, Z.L. Yu, Preparation and characterization of CNTs-TiO2 composites, Powder Technology, 154 (2005) 70-72.
[34] N.I. Kovtyukhova, T.E. Mallouk, L. Pan, E.C. Dickey, Individual single-walled nanotubes and hydrogels made by oxidative exfoliation of carbon nanotube ropes, Journal of the American Chemical Society, 125 (2003) 9761-9769.
[35] M.H. Liu, Y.L. Yang, T. Zhu, Z.F. Liu, Chemical modification of single-walled carbon nanotubes with peroxytrifluoroacetic acid, Carbon, 43 (2005) 1470-1478.
[36] B. Guo, Z.R. Qiu, K.S. Wong, Intensity dependence and transient dynamics of donor-acceptor pair recombination in ZnO thin films grown on (001) silicon, Applied Physics Letters, 82 (2003) 2290-2292.
[37] H.B. Fan, S.Y. Yang, P.F. Zhang, H.Y. Wei, X.L. Liu, C.M. Jiao, Q.S. Zhu, Y.H. Chen, Z.G. Wang, Investigation of oxygen vacancy and interstitial oxygen defects in ZnO films by photoluminescence and x-ray photoelectron spectroscopy, Chinese Physics Letters, 24 (2007) 2108-2111.
[38] Z.H. Lim, A. Lee, Y. Zhu, K.Y. Lim, C.H. Sow, Sustained laser induced incandescence in carbon nanotubes for rapid localized heating, Applied Physics Letters, 94 (2009).

[39] G. N. N., E. A., Chemistry of the Elements, Second ed., Butterworth-Heinemann, 1997.
[40] M. Wasik, A. Duzynska, J. Judek, M. Pawowski, K. Switkowski, A.M. Witowski, M. Zdrojek, Ultraviolet to far-infrared transmission properties of thin film multi-walled carbon nanotube random networks, Journal of Materials Science, 52 (2017) 3086-3094.
[41] S.X. Lim, S.L. Chang, F.C. Cheong, E.S. Tok, Z. Zhang, C.T. Lim, C.H. Sow, Field Emission from Decorated Carbon Nanotube-QDs Microstructures with a View to the Dominant Electron Paths, Journal of Physical Chemistry C, 117 (2013) 14408-14417.
[42] X.D. Lim, Y.W. Zhu, B. Varghese, X.Y. Gao, A.T.S. Wee, C.H. Sow, Re-Grown Aligned Carbon Nanotubes with Improved Field Emission, Journal of Nanoscience and Nanotechnology, 12 (2012) 258-266.

Zhong Wei Isaac Kwek, Yi Jie Valerie Tan, Zheng Zhang, Chorng-Haur Sow*, Sharon Xiaodai Lim*

Scintillating Zinc Oxide Ensconced in a Carbon Nanotube Forest Engineered by Laser Micro-Welding

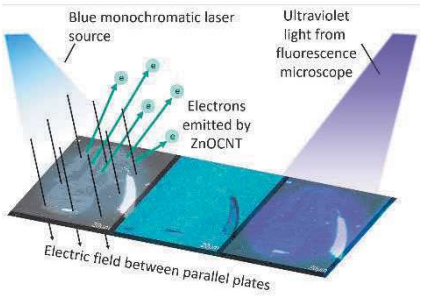

Supporting Information

Scintillating Zinc Oxide Ensconced in a Carbon Nanotube Forest Engineered by Laser Micro-Welding

Zhong Wei Isaac Kwek, Yi Jie Valerie Tan, Zheng Zhang, Chorng-Haur Sow*, Sharon Xiaodai Lim*

1 Contents of this supplementary file:

Section S1. Systematic study – sputtering and characterisation

Figure S1 contains a schematic of the sputtering process (Figure S1(a)), as well as top view and side view SEM images depicting the physical appearance of the CNT sample before and after undergoing the sputtering process (Figure S1(b)). After the sputtering procedure, large clumps of Zn particles are observed to agglomerate at the top of the CNT array. A 3-D profile of the sputtered Zn layer, captured *via* AFM, is presented in Figure S1(c), and the thickness of the Zn layer is measured to be 219 nm. The presence of Zinc, Carbon and Oxygen in the hybrid system is confirmed by an EDX elemental map (Figure S1(d)).

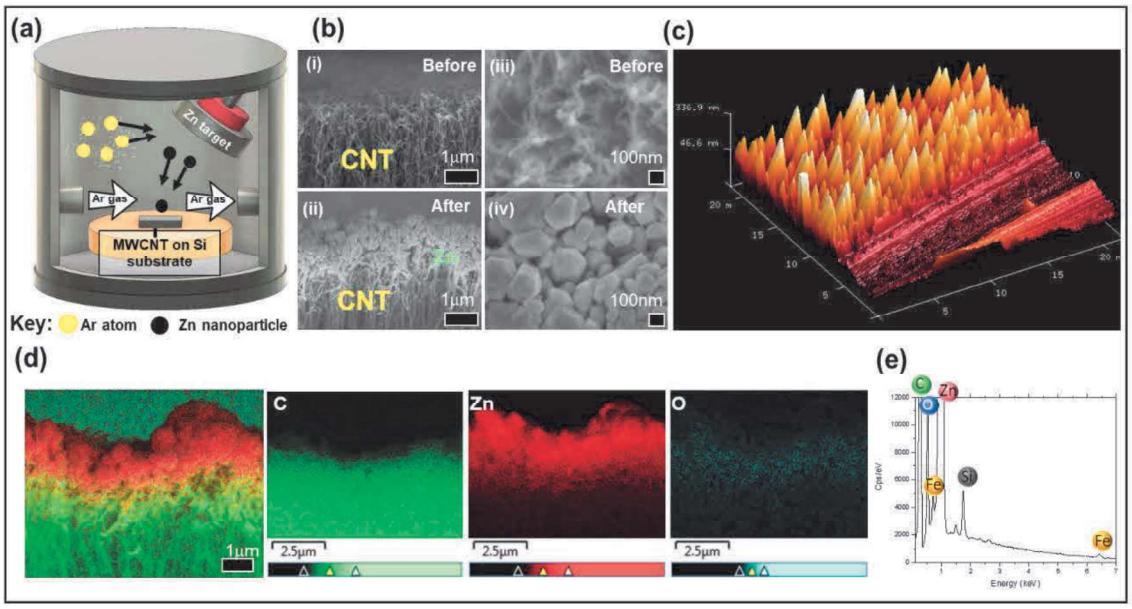

Figure S1. (a) Schematic diagram of sputtering process for deposition of Zn nanoparticles onto CNT array. (b) Scanning electron microscopy (SEM) images of CNT array (i, iii) before and (ii, iv) after sputtering process. (c) Three-dimensional (3D) tilted AFM height profile of Zn layer sputtered onto Si substrate. (d) Energy-dispersive X-ray (EDX) spectroscopy elemental mapping of (i) Zn, C and O, (ii) Zn, (iii) C and (iv) O in hybrid system. (e) EDX spectrum.

Section S2. Systematic study – Effect of laser patterning speed and power on fluorescence of ZnCNT hybrid

The rationale for choosing a patterning speed of 50µm s^{-1} is two-fold. Firstly, the emission of both violet and green fluorescence by a square region modified using a laser power of 9 mW and a patterning speed of 50µm s^{-1} under UV excitation signifies its importance as a transition phase is present. Secondly, the uniformity of the fluorescence emitted by the squares modified using a patterning speed of 50µm s^{-1} indicates the uniform formation of ZnO, rendering them ideal candidates for further investigation. The transition of the fluorescence colour from violet to green when the laser power increased from 7 to 11mW at a constant speed of 50µm s^{-1} imbues these parameters with particular importance, for they bear out the fact that a clear correlation exists between the laser powers, patterning speed and the properties of the ZnOCNT nanohybrid.

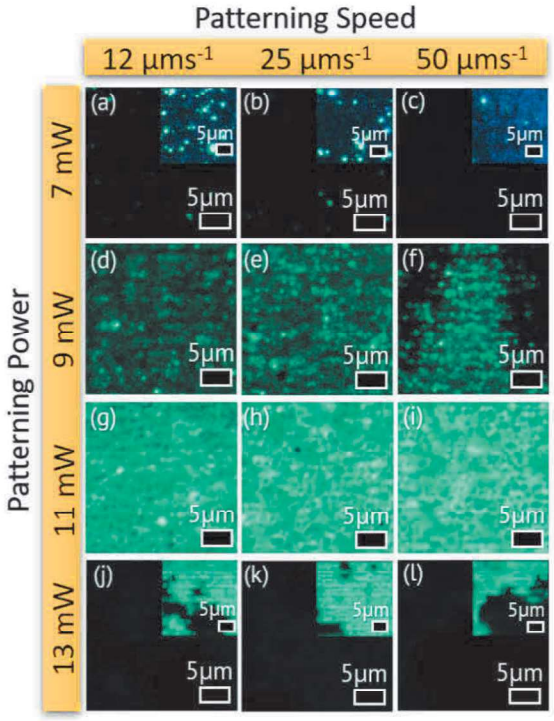

Figure S2. Systematic study on the effect of laser patterning and power on the fluorescence of ZnCNT hybrid system under UV excitation. All images were taken at the same exposure. Due to weaker fluorescence for samples patterned at 7 mW and 13 mW, brightness and contrast were adjusted to better showcase the fluorescence colour. The adjusted images are presented as insets of the respective original images.

Section S3. XPS of ZnCNT

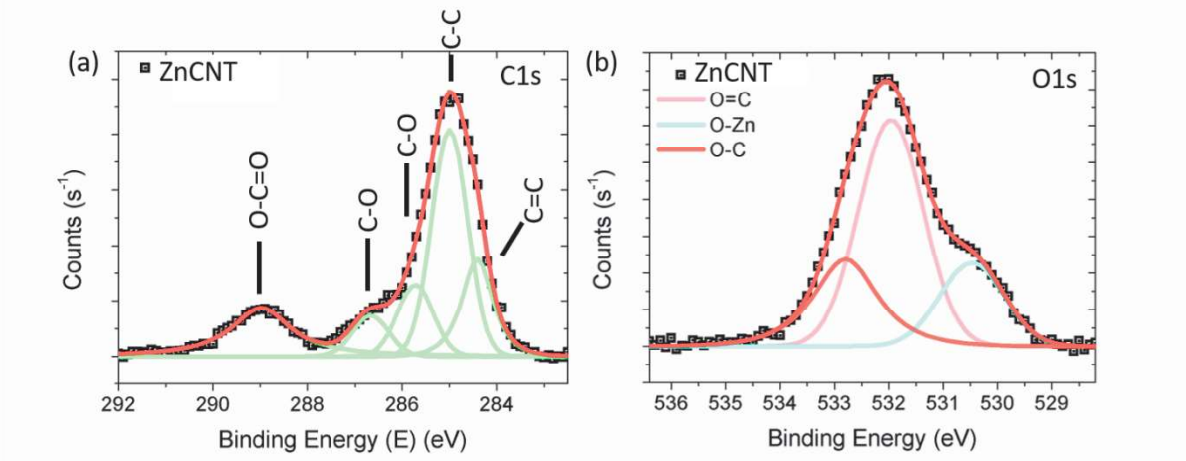

Figure S3. XPS analysis of (a) C 1s and (b) O 1s peaks of pristine ZnCNT sample.

Section S4. The role of CNTs and thickness of the Zn coating on the observed fluorescence

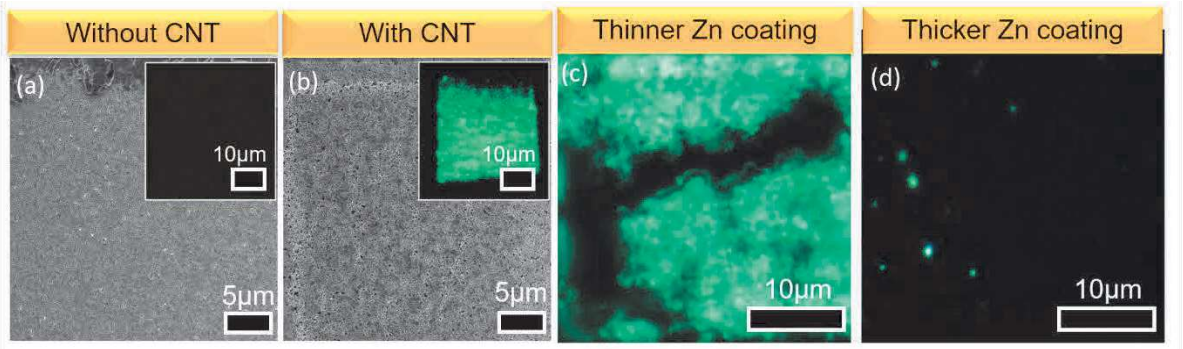

Figure S4. (a-b) SEM and FM (inset) showing the critical role that CNTs play in assisting the laser-initiated site-selective fluorescence of the hybrid material. (c-d) Green fluorescence being observed from CNTs array with thinner Zn coating, after being treated with the same laser power.

Section S5. Environmental control during the laser patterning process

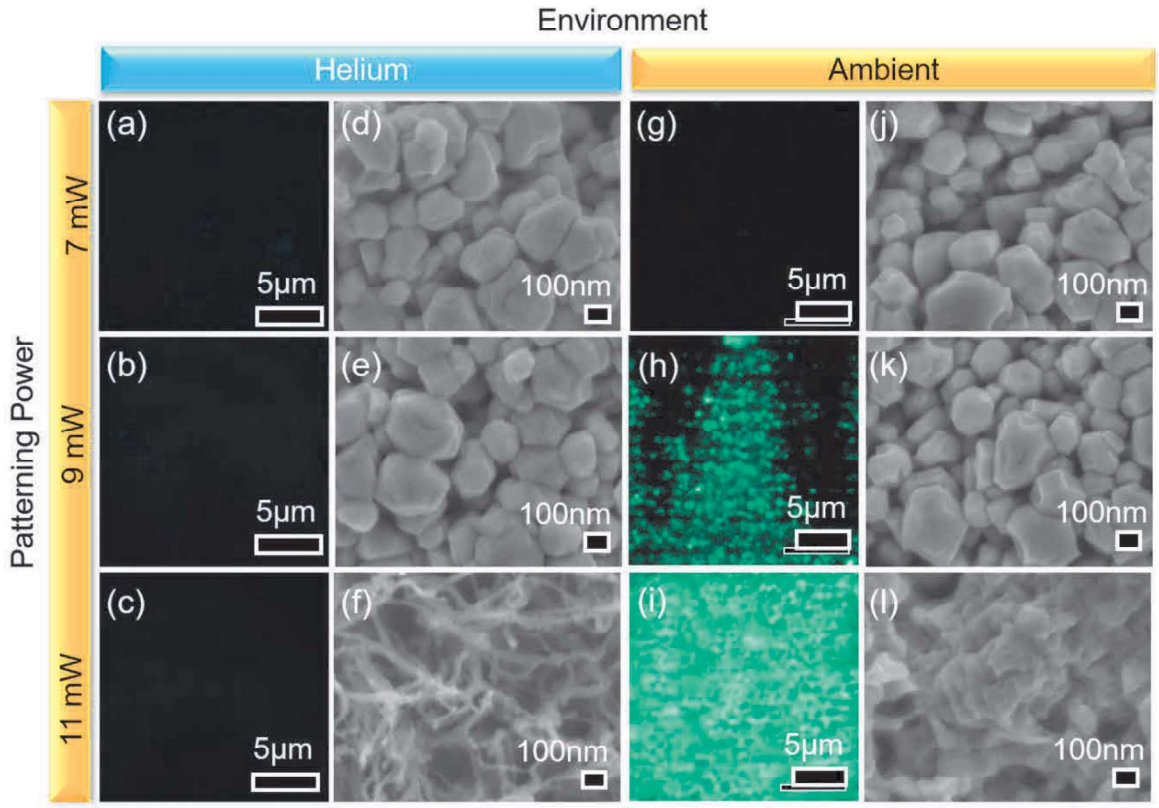

Figure S5. (a-c; g-i) FM and (d-f; j-l) SEM images of ZnOCNT samples patterned using (a,d, g, j) 7mW, (b, e, h, k) 9mWand (c,f, i, l) 11mW laser power in (a-f) helium (He) and (g-l) ambient environment.

Section S6. Field emission setup

The FE measurement is conducted using a top-down electrode setup with a 200μm spacer.[42] The top electrode comprises phosphorous coated ITO glass-slides, such that green fluorescence will be observed from regions interacting with the emitted electrons. Two sets of experiments are repeated, and the trend observed is found to be repeatable. Figure S6(a-b) shows a schematic of the field emission chamber and the setup used for field emission measurements.

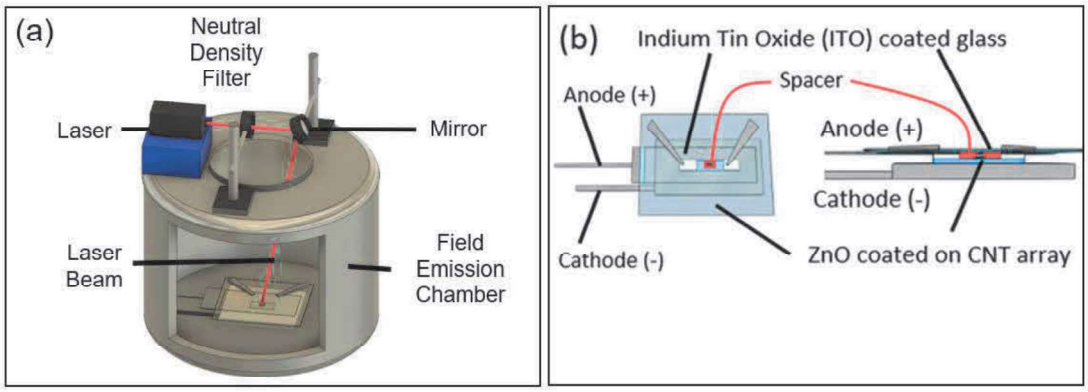

Figure S6. (a, b) Schematic diagram of field emission setup.

Section S7. Field emission mechanism and field emission current *vs* voltage plot

Detailed SEM characterisation of the samples (Figure 6(b-e)) reveals a possible correlation between the surface morphologies of the samples and their field emission properties (Figure 6(a) and Figure S7). We propose the following as a possible explanation for the observed phenomena: agglomeration of Zn nanoparticles in ZnCNT (Figure 6(b)) due to the high surface energy of Zn causes ZnCNT to have a reduced aspect ratio with rounded edges. The rounded edges augment the screening effect, inhibiting field emission from the CNTs concealed beneath the surface. As a result, the enhancement factor is the lowest value among the four types of samples tested.

With regards to the $ZnOCNT_V$ (Figure 6(c)) sample, as mentioned earlier and portrayed in Figure 3(b-d), the lattice lines on the nanoparticles present in $ZnOCNT_V$, $ZnOCNT_{VG}$ and $ZnOCNT_G$ become increasingly defined from $ZnOCNT_V$ to $ZnOCNT_G$. The differences in the definitions of the lattice lines support the claim that the former contains amorphous ZnO, while the latter contains crystalline ZnO. The poorly defined energy levels in the amorphous ZnO nanoparticles present in $ZnOCNT_V$ inhibit the effective emission of electrons from the hybrid structure, thus accounting for its poor field emission properties.

On the other hand, ablation by the FLB causes the ZnO nanoparticles in $ZnOCNT_{VG}$ (Figure 6(d)) and $ZnOCNT_G$ (Figure 6(e)) to be more crystalline. The ablation process improves their aspect ratios, creating more clearly defined edges (as indicated by the arrows), and ameliorates the screening effect. This enables them to act as additional emitter points that effectively enhance the field emission properties of the nanohybrids. With a lower work function compared to the $ZnOCNT_{VG}$ samples, electrons are more likely to be emitted from

$ZnOCNT_G$ under the same applied potential. The field emitting properties of $ZnOCNT_G$, can be further enhanced with the exposure of underlying CNTs (indicated by the green arrow in Figure 6(e)), which reduces the screening effect between the ZnO nanoparticles. Although CNTs can also serve as potential field emitters, under a similar condition, electron emissions from ZnO nanoparticles will take place more readily. This is due to the work function of $ZnOCNT_{VG}$ and $ZnOCNT_G$, which has a value of 4.22eV and 4.20eV, being much lower than the work function of CNT, 4.90eV.[41]

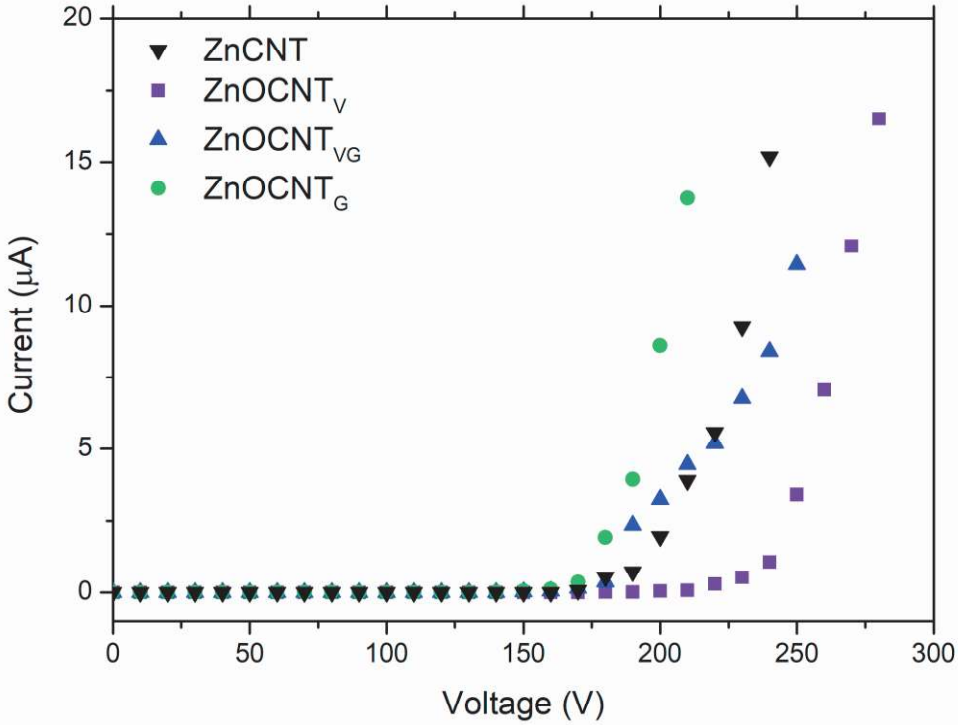

Figure S7. Current *vs* voltage field emission plot of ZnCNT, $ZnOCNT_V$, $ZnOCNT_{VG}$ and $ZnOCNT_G$ respectively.

Section S8. Field enhancement factor from the Fowler-Nordheim (FN) plot

The field enhancement factor of the various samples are determined based on the Fowler-Nordheim (F-N) equation:

$$J = \frac{AF^2}{\phi} \exp\left(-\frac{B\phi^{\frac{3}{2}}}{F}\right) \quad (1)$$

Here, F (= βE) is the local electric field (Vcm^{-1}), E is the applied field, β is the enhancement factor, ϕ is the work function (eV), J (= I γ^{-1}) is current density, where I is the total current from the measurement and γ is the effective area of emission. A and B are constants with respective values being 1.4 x 10^{-6} AeV V^{-2} and 6.44 x 10^7 V $eV^{-3/2}$ cm^{-1}. Rearranging equation (1), we arrive at the following relationship:

$$\ln\left(\frac{J}{E^2}\right) = \left(-\frac{B\phi^{\frac{3}{2}}}{\beta}\right)\left(\frac{1}{E}\right) + \ln\left(\frac{A\beta^2}{\phi}\right) \quad (2)$$

Equation (2) suggests that plotting $\ln(J/E^2)$ to 1/E (termed as an FN plot, inset of Figure 6(a)), the enhancement factor or work function of the material can be determined from the gradient of the graph

Section S9. UPS analysis

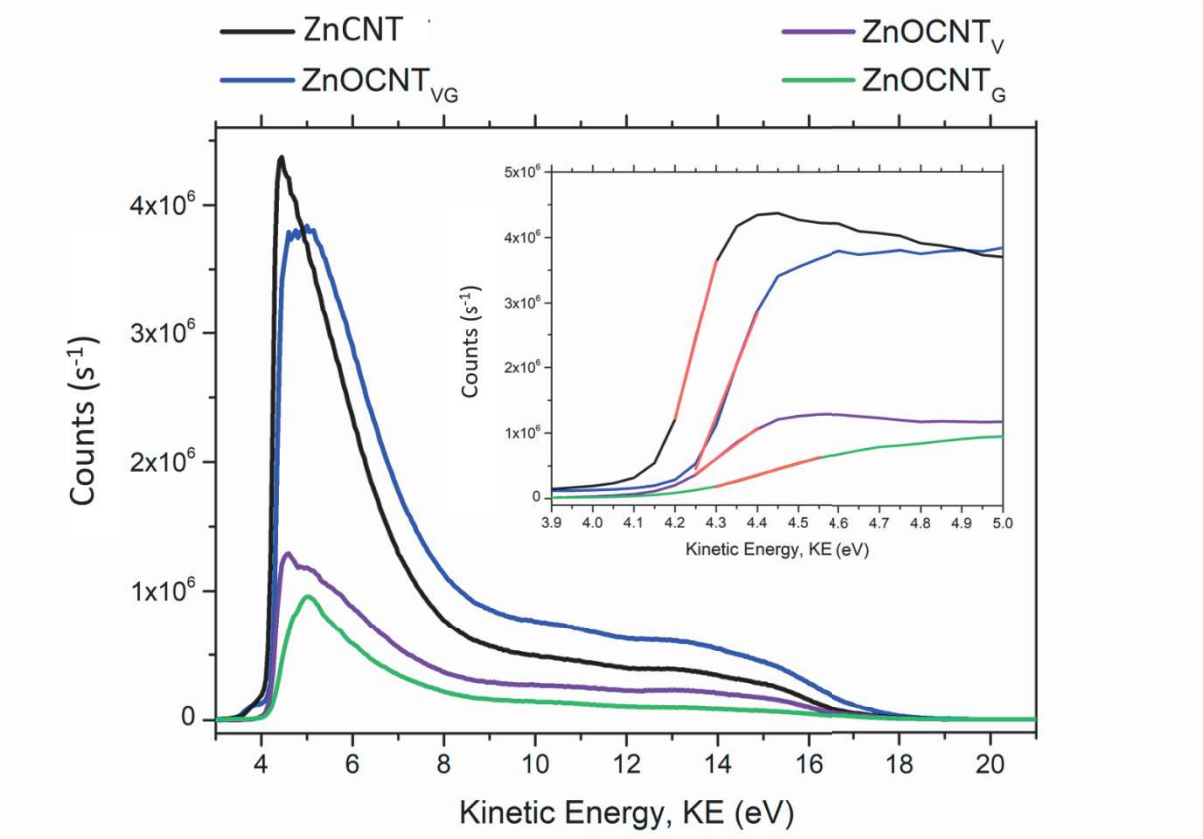

Figure S9. UPS analysis of ZnCNT, ZnOCNT$_V$, ZnOCNT$_{VG}$ and ZnOCNT$_G$. Inset shows a magnified view of the cut off point, where extrapolation reveals the work function of the individual hybrid material.